

New Explorations on Cannon's Contributions and Generalized Solutions for Uniform Linear Motion Blur Identification

Lu Wang¹ (王 璐), Hong-Yan Zhang^{2,3} (张鸿燕), and Si-Long Peng¹ (彭思龙)

¹The National Engineering and Technology Research Center for ASIC Design, Institute of Automation, Chinese Academy of Sciences, Beijing 100190, China

²The Key Laboratory of Complex Systems and Intelligence Science, Institute of Automation, Chinese Academy of Sciences Beijing 100190, China

³Sino-European Institute of Aviation Engineering, Civil Aviation University of China, Tianjin 300300, China

E-mail: lu.wang@ia.ac.cn; hongyan.siae@gmail.com; silong.peng@ia.ac.cn

Received June 3, 2011; revised September 8, 2011.

Abstract Existing frequency-domain-oriented methods of parameter identification for uniform linear motion blur (ULMB) images usually dealt with special scenarios. For example, blur-kernel directions were horizontal or vertical, or degraded images were of foursquare dimension. This excludes those identification methods from being applied to real images, especially to estimate undersized or oversized blur kernels. Pointing against the limitations of blur-kernel identifications, discrete Fourier transform (DFT)-based blur-kernel estimation methods are proposed in this paper. We analyze in depth the Fourier frequency response of generalized ULMB kernels, demonstrate in detail its related phase form and properties thereof, and put forward the concept of *quasi-cepstrum*. On this basis, methods of estimating ULMB-kernel parameters using amplitude spectrum and quasi-cepstrum are presented, respectively. The quasi-cepstrum-oriented approach increases the identifiable blur-kernel length, up to a maximum of half the diagonal length of the image. Meanwhile, directing toward the image of undersized ULMB, an improved method based on quasi-cepstrum is presented, which ameliorates the identification quality of undersized ULMB kernels. The quasi-cepstrum-oriented approach popularizes and applies the simulation-experiment-focused DFT theory to the estimation of real ULMB images. Compared against the amplitude-spectrum-oriented method, the quasi-cepstrum-oriented approach is more convenient and robust, with lower identification errors and of better noise-immunity.

Keywords Fourier amplitude spectrum phase, perpendicular relation, uniform linear motion, blur identification, quasi-cepstrum

1 Introduction

There exist many degradation factors in a practical imaging system. Some factors affect gray-level values of individual image pixels, and others lead to the blurring of the whole image. For instance, the motion blur occurs when the image-acquisition equipment and the targeted objects are relatively moving. Uniform linear motion (ULM)^[1] is the simplest kind of motion and the generic motion at variable speed or of non-linearity can be decomposed into piecewise ULM. Therefore, blur recognition and image reproduction that concern the ULM are still of common significance.

The uniform linear motion blur (ULMB) is signified

by two parameters: 1) the angle between the motion and the horizontal axis, i.e., the direction of the motion; 2) the spreading extent along the motion direction, i.e., the length of the motion. The existing parameter-identifying approaches can be divided into two categories. One is based on image statistics, and the other is based on Fourier analysis.

The first category^[2-3] copes with the original image with the spatially isotropic first-order Markov stochastic process, where the motion blur decreases high-frequency contents of the image along the motion direction while having less effect upon those contents along other directions. Since the blurred image has the least high frequency contents along the motion direction,

Regular Paper

The work is supported in part by the National Natural Science Foundation of China under Grant Nos. 61032007, 60972126 and 60921061, the Joint Funds of the National Natural Science Foundation of China under Grant No. U0935002/L05, and the Natural Science Foundation of Beijing under Grant No. 4102060.

©2012 Springer Science + Business Media, LLC & Science Press, China

most of the energy will be lost if a high pass filtering process (directional derivation) is taken. The motion blur is detected in three steps:

- 1) measure the direction where the total intensity of the image derivative is the lowest;
- 2) calculate the autocorrelation of the derivative image that is obtained along the identified direction, and summate columns of it to get a curve;
- 3) find the blur length, which is just half the distance between the two symmetrical negative peaks of the obtained curve.

Although this kind of methods is acceptable for blur length estimation along the horizontal or the vertical directions, it is complicated for the blur direction identification. Its estimation formulae for directional angles vary in accordance with which part of the eight equant sectors that the angle belongs to in the rectangular coordinates.

The second category can be divided into four subtypes.

1) Amplitude Spectrum (AS) Analysis Approach. For example, the motion direction is first estimated by Radon transform^[4-5], Hough transform^[6], or Gabor transform^[7], and then the motion length along the direction is identified.

2) Cepstrum Analysis Approach^[8-11]. A cepstrum is defined as the (inverse) Fourier transform of the log AS. The cepstral equispaced negative spikes and the angles that they have been rotated indicate the motion-blur parameters. Besides, Cannon^[8] presented an AS-related proposition for blur kernel identification.

3) Bispectrum Analysis Approach^[12]. A bispectrum is a three-order spectrum, constructed on the multiplying basis of spectra, and is employed to recognize the motion length when the motion direction is known.

4) Discrete cosine transform (DCT) Spectrum Analysis Approach^[13]. A DCT^[14] expresses a sequence of finitely many data points in terms of a sum of cosine functions of varying amplitudes and oscillating at different frequencies. The existing method is only employed to estimate the motion length along the horizontal or the vertical motion direction.

The ULMB identifying principle behind the AS-oriented methods^[4-7] and the AS proposition mentioned in Cannon's paper^[8] are actually identical. The researchers got used to consider particular situations to evaluate AS properties, in which the spectra that have dimensions equal to those of their input images are square-shaped, or the blur kernels are horizontal or vertical. Although this AS method works well and truly for the cases they illustrated, it is in fact not complete. These factors makes this method involve in synthetic experiments only. Through stringent mathematical

descriptions, we extend the current AS-based identification method to more generic scenarios.

Let us expand forward upon the cepstrum analysis method. Cannon^[8] broke up the entire image into one or two hundred (possibly overlapping) subsections, each being large enough to contain the point spread function (PSF). An average was taken over the power cepstrum of each subsection so as to take advantage of cepstral spikes to detect blur parameters. In [9], Fabian *et al.* first employed a form of spectral subtraction method for noise suppression, and then they transformed the enhanced spectral magnitude function to the cepstral domain and identified the PSF using an adaptive quefrequency-varying comb-like window lifter. Wu *et al.*^[10] adopted an edge detector (Sobel or Canny operator) to convert the cepstrum image into the binary image for the purpose of extracting the motion direction by Hough transform. Then, after extracting the cross-section values in motion direction, they interpolated the logarithm spectrum to detect the motion length. The procedures for those methods are quite complicated and fussy. Xie *et al.*^[11] first removed the noise from the blurred image, and improved cepstral calculations of the image on the basis of the Fourier frequency spectrum. And then, they found the minimal values of the cepstrum, which just reflected the information of blur-kernel parameters. However, this method is suitable only for parameter estimations for blur kernels whose blur length is within 10 to 50 pixels and it would fail when the blur length is smaller than 5 pixels or larger than 55 pixels. At the same time, all these estimation methods are often implemented in synthetically experimental images, and have not been performed with an eye to the identification problems of undersized and oversized blur kernels that exist in real-world images. To address this shortcoming, we make an improvement in order to better utilize the features of the cepstrum for the ULMB detection and image recovery. By our efforts, the theory for ULMB kernel identification by the discrete Fourier transform (DFT) is better established, and the reliability and the applicability of the DFT-based identification methods for treating real-world blurred images is improved considerably.

The remainder of the paper reads as follows. In Section 2, we explain some basic mathematical concepts, and Cannon's contributions are revisited in Section 3. The detailed mathematical proof of the AS-related proposition is accompanied in Section 4. We then present a modified version of the cepstrum that ameliorates the quality of kernel recognition in Section 5, and Section 6 provides experimental results, and finally, Section 7 gives some concluding remarks.

2 Mathematical Preliminaries

2.1 DFT

The two-dimensional (2D) DFT^[15] of a function (image) $G(x, y)$ is defined as

$$\mathcal{G}(p, q) = \text{DFT}\{G(x, y)\} = \sum_{x=0}^{X-1} \sum_{y=0}^{Y-1} G(x, y) \cdot e^{-j\frac{2\pi}{P}px} \cdot e^{-j\frac{2\pi}{Q}qy}, \quad (1)$$

where x and y are the image or spatial variables, and $p \in \{0, \dots, P-1\}$ and $q \in \{0, \dots, Q-1\}$ are the transform or frequency variables. In addition, $X \cdot Y$ is the size of the domain of the spatial function $G(x, y)$, and $P \cdot Q$ is the size of the domain of the frequency function $\mathcal{G}(p, q)$.

2.2 Cepstrum

The cepstrum^[8] of $G(x, y)$ is defined as

$$\mathfrak{C}(u, v) = \text{Ceps}\{G(x, y)\} = \text{DFT}\{\log(|\mathcal{G}(p, q)|)\} = \sum_{p=0}^{P-1} \sum_{q=0}^{Q-1} [\log(|\mathcal{G}(p, q)|)] \cdot e^{-j\frac{2\pi}{U}vp} \cdot e^{-j\frac{2\pi}{V}vq}, \quad (2)$$

where $u \in \{0, \dots, U-1\}$ and $v \in \{0, \dots, V-1\}$ are the quefrency domain variables. $|\cdot|$ stands for the absolute value, and $\log(\cdot)$ represents the log transformation^[16].

2.3 ULMB Kernel

The ULMB kernel can be regarded as a two-variable rectangular window^[15], which is defined by

$$K(x, y) = \begin{cases} \frac{1}{L}, & (x, y) \in \ell_{AB}, \\ 0, & \text{otherwise,} \end{cases} \quad (3)$$

$$\sum_x \sum_y K(x, y) = 1, \quad (4)$$

$(x, y) \in \text{Supp}(K)$

in which ℓ_{AB} is a section of line along $y = (\tan \theta) \cdot x + c$, c is a constant. The support set of $K(x, y)$ is displayed in (4),

$$\text{Supp}(K) = \{(x_i, y_i) | x_i = i \cos \theta, y_i = i \sin \theta + c, l \leq i \leq l + L - 1, l \in \mathbb{Z}\}, \quad (4)$$

where L denotes the length of the kernel as well as the number of sampling points upon this rectangular window, θ is its direction off x axis within the range $(-\frac{\pi}{2}, \frac{\pi}{2}]$, and $\Delta x = \cos \theta$ and $\Delta y = \sin \theta$ are sampling intervals along x and y axes, respectively.

3 Cannon's Contributions Revisited

3.1 Contributions

Cannon has made two contributions in his published paper^[8]. First, he introduced a power spectrum equalization filter for image restoration in the presence of noise as well as a technique in quefrency domain to detect joint spatially invariant ULMB and out-of-focus blur. The second contribution is that he brought out a proposition on the zero crossings of the frequency response of the ULMB system from which the motion parameters could be identified. This identifying principle has been referred by some subsequent researchers, such as [4-7].

In Cannon's paper, the 2D frequency response of the ULMB system is

$$\mathcal{H}(p, q) = \frac{\sin(\pi L \sigma)}{\pi L \sigma}, \quad (5)$$

where $\sigma = p \cos \theta + q \sin \theta$. He supposed the total frequency length to be 1, and believed that the zeros of this response occurred along lines perpendicular to the direction of blur and those zeros were spaced at intervals of $d = \frac{1}{L}$. That is to say, the amplitude of (5) is characterized by periodic zeros on the spectral p axis, which occur at

$$p = \frac{\kappa}{L}, \quad \kappa = \pm 1, \pm 2, \dots, \quad (6)$$

$$d = \Delta p = \frac{1}{L}. \quad (7)$$

Intuitively, if the blur is horizontal ($\theta = 0$) or vertical ($\theta = \frac{\pi}{2}$), and the frequency length is enlarged by a scale of P or Q , which is the spectral order along p or q axis, (5) and (7) will be simplified, respectively, into

$$\mathcal{H}(p) = \frac{\sin(\pi L p)}{\pi L p}, \quad \Delta p = \frac{1}{L}, \quad d_p = \frac{P}{L}, \quad (8)$$

$$\mathcal{H}(q) = \frac{\sin(\pi L q)}{\pi L q}, \quad \Delta q = \frac{1}{L}, \quad d_q = \frac{Q}{L}. \quad (9)$$

3.2 Remarks

We notice that Cannon *et al.* examined mainly standard or other images that are square-shaped, like Baboon, Cameraman, and Lena, convolved by prescribed kernels. However, rectangular-shaped images are more popular in reality, e.g., shake blurred photos taken by regular cameras. The ratio of width to height of the captured images are usually 4:3, and sometimes 3:2 or 16:9. Mathematically, the square is just a special rectangle. If spectral orders along horizontal and vertical axes, respectively, are assigned equally to spatial dimensions of the image, the identifying principle applied

to rectangular-shaped images is different from that of those square-shaped images. Subsection 4.2 will clarify the influence factors of the Fourier spectrum and how X , Y , P and Q play their roles in the spectrum.

From a historical viewpoint, Cannon's proposition still makes sense in specific circumstances. In a perspective of development, a panorama of the theory connecting the Fourier spectrum and the ULMB is also worthy of being discovered, which is only partially interpreted in previous literature. Through comparisons between particularity and generalization, we gain more insights into this topic. Regarding the standard cepstrum, we provide a revised form as well, which helps to extend the scope of its application.

4 General Solution in Frequency Domain

4.1 Image Degradation Model

The image degradation model frequently adopted is

$$B = K \circledast S + N, \quad (10)$$

where B is the blurred image, K is the PSF or the blur kernel, S is the original sharp scene, and N is the additive noise. When noise is neglected, (10) becomes

$$B = K \circledast S. \quad (11)$$

With the help of the convolution theorem, we get

$$B = \mathcal{K} \cdot S, \quad (12)$$

where \mathcal{B} , \mathcal{K} and \mathcal{S} stand for the DFT of B , K and S , respectively. Thus for a fixed latent sharp image S , once \mathcal{K} is decided, the blurred image B can be restored from \mathcal{K} . This implies that we can put the emphasis on $\mathcal{K} = \text{DFT}\{K\}$.

4.2 DFT of ULMB Kernel

4.2.1 Basic Expressions

To take the DFT of the kernel $K(x, y)$, according to (1) and (4), we derive

$$\begin{aligned} \mathcal{K}(p, q) &= \text{DFT}\{K(x, y)\} \\ &= \sum_x \sum_y K(x, y) \cdot e^{-j\frac{2\pi}{P}px} \cdot e^{-j\frac{2\pi}{Q}qy} \\ &= \frac{1}{L} \cdot \sum_{i=l}^{l+L-1} e^{-j\frac{2\pi}{P}pi \cos \theta} \cdot e^{-j\frac{2\pi}{Q}q(i \sin \theta + c)}, \\ &= e^{-j\frac{2\pi}{Q}qc} \cdot \frac{1}{L} \cdot \sum_{i=l}^{l+L-1} \left[e^{-j2\pi\left(\frac{p \cos \theta}{P} + \frac{q \sin \theta}{Q}\right)i} \right], \\ &\quad l \in \mathbb{Z}. \end{aligned} \quad (13)$$

Let

$$\begin{aligned} \mu &= 2\pi \cdot \frac{qc}{Q}, \\ \omega &= 2\pi \cdot \left(\frac{p \cos \theta}{P} + \frac{q \sin \theta}{Q} \right), \end{aligned} \quad (14)$$

and on the basis of the partial sum rule of geometric series^[17], (13) can be written by

$$\begin{aligned} \mathcal{K}(\mu, \omega) &= e^{-j\mu} \cdot \frac{1}{L} \cdot \sum_{i=l}^{l+L-1} (e^{-j\omega})^i \\ &= e^{-j\mu} \cdot \frac{1}{L} \cdot (e^{j\omega})^l \cdot \sum_{i=0}^{L-1} (e^{-j\omega})^i \\ &= e^{-j\mu} \cdot e^{jl\omega} \cdot \frac{1}{L} \cdot \frac{1 - e^{-jL\omega}}{1 - e^{-j\omega}} \\ &= e^{-j(l\omega - \mu)} \cdot \frac{1}{L} \cdot \frac{e^{-j\frac{L\omega}{2}}}{e^{-j\frac{\omega}{2}}} \cdot \frac{e^{j\frac{L\omega}{2}} - e^{-j\frac{L\omega}{2}}}{e^{j\frac{\omega}{2}} - e^{-j\frac{\omega}{2}}} \\ &= e^{-j(l\omega - \mu)} \cdot e^{-j\frac{(L-1)\omega}{2}} \cdot \frac{1}{L} \cdot \frac{\sin \frac{L\omega}{2}}{\sin \frac{\omega}{2}}, \quad l \in \mathbb{Z}. \end{aligned} \quad (15)$$

The AS, viz., the modulus, of $\mathcal{K}(\mu, \omega)$ is

$$|\mathcal{K}(\omega)| = \frac{1}{L} \left| \frac{\sin \frac{L\omega}{2}}{\sin \frac{\omega}{2}} \right|, \quad (16)$$

where L is a constant positive integer specifying the length of the line segment. Obviously, if $\frac{L\omega}{2} = z\pi$ ($z \neq 0$), then $\left| \sin \frac{L\omega}{2} \right| = 0$ and $|\mathcal{K}(\omega)| \equiv 0$. Furthermore, according to the calculus of limits^[17], if $\omega \rightarrow 0$, we can obtain

$$\lim_{\omega \rightarrow 0} |\mathcal{K}(\omega)| = \lim_{\omega \rightarrow 0} \frac{1}{L} \left| \frac{\sin \frac{L\omega}{2}}{\sin \frac{\omega}{2}} \right| = 1. \quad (17)$$

Hence, we obtain the conditions for the central bright stripe and sidelobe dark stripes of $|\mathcal{K}(\omega)|$ as follows.

$$\text{Central bright stripe: } \frac{L\omega}{2} = 0, \quad (18)$$

$$\text{Sidelobe dark stripes: } \frac{L\omega}{2} = z\pi, \quad z = \pm 1, \pm 2, \dots \quad (19)$$

By substituting (14) into (18) and (19), we immediately get

$$\frac{p \cos \theta}{P} + \frac{q \sin \theta}{Q} = \frac{z}{L}, \quad z \in \mathbb{Z}. \quad (20)$$

This is the most important result for the parallel AS stripes of the ULMB and the generalized expression to be determined.

What needs our attention is that $K(x, y)$, $\text{Supp}(K)$, P , and Q are by nature all indispensable to properly determine $\mathcal{K}(p, q)$. P and Q here are the sizes of the DFT output along p and q axes. All those stripes, originally, have nothing to do with the size of input images. Nevertheless, for the transformation from (11) to (12) to make sense, the order of the transform ought to be at least the dimension of the image. In other words, $P \geq X$ and $Q \geq Y$. If not, the spectrum will not take into account the intact information of the original image, meaning that the spectral information will be partially lost. Equalities of $P = X$ and $Q = Y$ (NOT $P = Q$) are normally selected. This choice agrees upon the nature of original images, too.

4.2.2 AS Direction

We define the angle ϕ off the horizontal axis as the AS direction of parallel stripes, as displayed in Fig.1. Geometrically, (20) represents a pencil of parallel lines with a common slope^[17].

$$\tan \phi = -\frac{\frac{\cos \theta}{\frac{P}{\sin \theta}}}{\frac{Q}{P \tan \theta}} = -\frac{Q}{P \tan \theta}, \quad \phi \in \left(-\frac{\pi}{2}, \frac{\pi}{2}\right], \quad (21)$$

which results in

$$\phi = -\arctan\left(\frac{Q}{P \tan \theta}\right), \quad \phi \in \left(-\frac{\pi}{2}, \frac{\pi}{2}\right]. \quad (22)$$

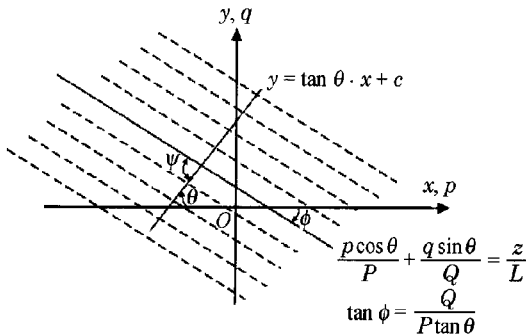


Fig.1. θ , ϕ and ψ .

4.2.3 Relationship Between AS Direction and ULMB Direction

Let

$$\psi = \theta - \phi \quad (23)$$

be the angle between the line ℓ_{AB} and the parallels described by (20), as displayed in Fig.1. In light of

properties of trigonometric functions^[17], we get

$$\begin{aligned} \psi &= \arctan\left(\frac{\tan \theta - \tan \phi}{1 + \tan \theta \cdot \tan \phi}\right) \\ &= \arctan\left(\frac{\tan \theta + \frac{Q}{P \tan \theta}}{1 - \frac{Q}{P}}\right). \end{aligned} \quad (24)$$

Let

$$f = \frac{\tan \theta + \frac{Q}{P \tan \theta}}{1 - \frac{Q}{P}}, \quad (25)$$

$$h = \frac{Q}{P}, \quad t = \frac{1}{\tan \theta}, \quad (26)$$

and we derive

$$f(h, t) = \frac{ht + \frac{1}{t}}{1 - h}. \quad (27)$$

The differentiation of (27) with respect to h implies

$$f'_h = \frac{\partial f}{\partial h} = \frac{t + \frac{1}{t}}{(1 - h)^2}. \quad (28)$$

We now analyze the angular relationship between AS stripes and ULMB, on the basis of properties of trigonometric functions, in the succeeding variant states:

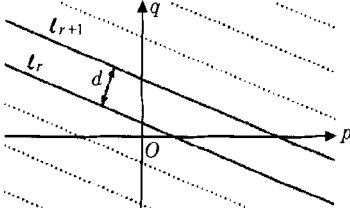
- 1) if $\theta \in (-\frac{\pi}{2}, 0)$, $\tan \theta < 0$, $\tan \phi > 0$, $f'_h < 0$, then $\phi \in (0, \frac{\pi}{2})$, and
 - if $h = \frac{Q}{P} = 1$, $\tan \psi \rightarrow -\infty$, then $\psi = -\frac{\pi}{2}$;
 - if $h = \frac{Q}{P} < 1$, then $\psi \in (-\frac{\pi}{2}, 0)$;
 - if $h = \frac{Q}{P} > 1$, then $\psi \in (-\pi, -\frac{\pi}{2})$;
- 2) if $\theta = 0$, $\tan \theta = 0$, $\tan \phi \rightarrow +\infty$, then $\phi = \frac{\pi}{2}$, and $\psi = -\frac{\pi}{2}$;
- 3) if $\theta \in (0, \frac{\pi}{2})$, $\tan \theta > 0$, $\tan \phi < 0$, $f'_h > 0$, then $\phi \in (-\frac{\pi}{2}, 0)$, and
 - if $h = \frac{Q}{P} = 1$, $\tan \psi \rightarrow +\infty$, then $\psi = \frac{\pi}{2}$;
 - if $h = \frac{Q}{P} < 1$, then $\psi \in (0, \frac{\pi}{2})$;
 - if $h = \frac{Q}{P} > 1$, then $\psi \in (\frac{\pi}{2}, \pi)$;
- 4) if $\theta = \frac{\pi}{2}$, $\tan \theta \rightarrow +\infty$, $\tan \phi = 0$, then $\phi = 0$, and $\psi = \frac{\pi}{2}$.

The results given above demonstrate that the direction of AS stripes of ULMB (specified by ϕ) are perpendicular to that of ULMB (specified by θ) only in three circumstances:

- 1) $\theta = 0$, $\forall P, Q$;
- 2) $\theta = \frac{\pi}{2}$, $\forall P, Q$;
- 3) $P = Q$, $\forall \theta$.

4.2.4 Adjacent Dark AS Interval

As displayed in Fig.2, we pick up two arbitrary

Fig.2. Illustration of d .

adjacent dark AS stripes, which are decided by the succeeding equations:

$$\begin{aligned} \ell_r : \frac{p \cos \theta}{P} + \frac{q \sin \theta}{Q} &= \frac{r}{L}, \\ \ell_{r+1} : \frac{p \cos \theta}{P} + \frac{q \sin \theta}{Q} &= \frac{r+1}{L}, \quad r = 1, 2, \dots \end{aligned} \quad (29)$$

Hence, the fringe spacing of AS stripes, namely, the distance of the two parallel lines^[17] ℓ_r and ℓ_{r+1} can be determined by

$$\begin{aligned} d &= \frac{\left| \frac{r}{L} - \frac{r+1}{L} \right|}{\sqrt{\left(\frac{\cos \theta}{P} \right)^2 + \left(\frac{\sin \theta}{Q} \right)^2}} \\ &= \frac{1}{L \sqrt{\left(\frac{\cos \theta}{P} \right)^2 + \left(\frac{\sin \theta}{Q} \right)^2}} \\ &= \frac{1}{L} \sqrt{\frac{P^2 \tan^2 \phi + Q^2}{\tan^2 \phi + 1}}. \end{aligned} \quad (30)$$

And the third expression is derived from (22). According to (30), the three particular circumstances happen as follows:

- 1) if $\theta = 0$, then $d = \frac{P}{L}$;
- 2) if $\theta = \frac{\pi}{2}$, then $d = \frac{Q}{L}$;
- 3) if $P = Q$, then $d = \frac{P}{L} = \frac{Q}{L}$.

4.3 Generalization of ULMB Identification

From (21) and (30), we derive the formulas in frequency domain for identifying the ULMB as listed below:

$$\begin{aligned} \theta &= -\arctan\left(\frac{Q}{P \tan \phi}\right), \quad \theta \in \left(-\frac{\pi}{2}, \frac{\pi}{2}\right], \\ L &= \frac{1}{d \sqrt{\left(\frac{\cos \theta}{P} \right)^2 + \left(\frac{\sin \theta}{Q} \right)^2}} = \frac{1}{d} \sqrt{\frac{P^2 \tan^2 \phi + Q^2}{\tan^2 \phi + 1}}. \end{aligned} \quad (32)$$

5 General Solution in Quasi-Quefrency Domain

5.1 Cepstrum and Quasi-Cepstrum of ULMB

In light of (2), the cepstrum of a two-variable function G is expressed as

$$\mathfrak{G} = \text{DFT}\{\log(|\mathcal{G}|)\}. \quad (33)$$

In the context of the ULMB kernel and image, Cannon and Fabian *et al.* declared that, in the (real-part) quefrency domain, along the motion direction, there is a pair of symmetrically distinct negative pulses at a distance of the motion length from the origin and replicas of these pulses at integer multiples of the length. The blur kernel can thus be recognized, and the blurred image recovered. Existing cepstrum-oriented kernel identification methods^[8-11] are complex and do not provide immediate results, and we attempt to tackle that.

In the similar manner of experiments, we discover that the stripe characteristics in the cepstrum-like domain acquired from the following formula (34) reveals the ULMB parameters more directly visible and succinctly. That is to say,

$$\mathbb{G} = \text{DFT}\{|\mathcal{G}|\}. \quad (34)$$

We define this cepstrum-like category as *quasi-cepstrum* (QC), and name the independent variable of a QC graph as the *quasi-quefrency* (QQ).

Learnt from the shape of the log curve, the log transformation maps a narrow range of low gray-level values in the input image into a wider range of output level. The opposite is true of higher levels of input values. Therefore, the log function is able to scale the large dynamic range of pixel values of the Fourier spectrum to more manageable numbers. After deleting the log transformation, the pixel values of the Fourier AS no longer spread or compress appropriately, and higher-order numbers outweigh low-level values and dominate the spectrum again. This change strengthens the central section and the first negative pulse pair of the cepstrum and weakens all the other replicated sidelobe spikes. In other words, in the (real-part) QQ domain of the ULMB system, along the motion direction, there exists a straight line segment, the pivot of which has the maximal gray-level value that descends to the minimum at the two endpoints; the pair of the darkest endpoints are located symmetrically at a distance of the motion length from the brightest pivot. For this reason, we call this graphic *quasi-twin-pointed map* (QTPM) of QC, and this characteristic graph in the original cepstrum *twin-pointed map* (TPM).

Comparisons of QC versus AS and standard cepstrum are displayed in Fig.3. The input images in the

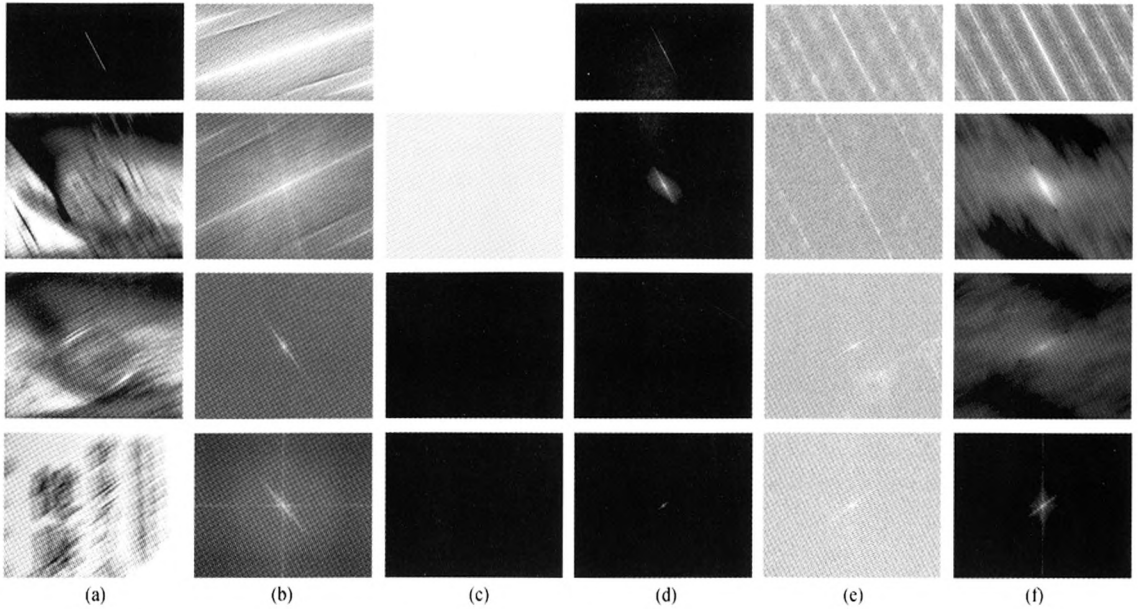


Fig.3. Comparisons of AS, cepstrum, and QC. (a) Input. (b) log AS. (c) Cepstrum. (d) QC. (e) log cepstrum. (f) log QC.

first column, from the first row to the last, are of pure PSF, of synthetic blur, of synthetic noisy blur, and real noisy blur, respectively. To be more visible, the log transformation is performed to the spectra, and their pixel intensities are normalized into $[0, 1]$. Towards the pure PSF image, the QTPM is sufficiently clear-cut within the QC, but for the blurred images, a log operation should be followed to acquire a more vivid QTPM.

Due to the noise effects, the search for zero crossings in the transformed graphs tends to fail. Nonetheless, it is worth noting that ULMB identification via the QQ domain is more robust and convenient than the frequency and quefrequency ones. The robustness means that even if the AS stripes or the cepstral spikes of the blurred image appear feeble or incomplete, the QTPM of its relevant QC remains legible and detectable. This superiority of QC over AS and standard cepstrum is especially prominent for real-world images, which are contaminated by some noise or with large blur length. From Fig.3, we also learn that 1) the AS of the noisy or actual photo is not as perfect as those of pure PSF and synthetic blur; 2) the cepstrum and its log version reduce to a midpoint and a central slope segment, respectively; 3) the QTPM of (log) QC is intact and still competent for seeking out the blur kernel information. The convenience signifies that only the two central darkest points of the QTPM are involved in computation rather than the overall transformed spectral data. Therefore, we prefer the QC technique in order to recognize and remove the ULMB, because this technique is

more straightforward, simpler and faster than the AS and the cepstrum approaches.

5.2 Generalization of ULMB Identification

In view of the preceding considerations, we propose an approach to recognize the ULMB kernels. In the (real-part) QC of the ULMB image, the coordinates of the dominant negative pulse pair of the QTPM are able to be detected, which we denote as (x_l, y_l) , for the left pair, and (x_r, y_r) , for the right one. In this scenario, the angle between the line segment and its projection onto the horizontal axis determines the motion direction, and the distance of the line segment between the two points decides the duplex motion length. In other words,

$$\theta = \arctan\left(\frac{y_r - y_l}{x_r - x_l}\right), \quad \theta \in \left(-\frac{\pi}{2}, \frac{\pi}{2}\right],$$

$$L = \frac{1}{2}\sqrt{(y_r - y_l)^2 + (x_r - x_l)^2}. \quad (35)$$

It should be noted that it is not so easy to recognize accurately the blur kernels of smaller angle and shorter length as compared to those with parameters of larger angle or longer length, e.g., when the estimated length is shorter than 15 pixels and its corresponding estimated angle is smaller than 10 degrees. We name this issue as the *small angle of short length problem* (SASLP). The *angle* here depicts angles of inclination against the vertical axis (y -axis) as well as those against the horizontal axis (x -axis). That is to say, the small

angles refer to angles in range of $(-90, -80]$, $[-10, 0)$, $(0, 10]$, or $[80, 90)$ degrees. That has something to do with the sampling rate along the blur length, and the customary sampling interval is one pixel. As the length increases, the number of pixels that is used to display the line segment within the QTPM in the QQ domain increases, which helps subtly depict the information of the kernel parameters. The opposite is true if the number of pixels along the length is too small to signify a slight angle deviation.

We attempt to handle this SASLP better for those ULMB kernels via the QQ domain. When we come across the situation that the first-pass detected parameters fall into the range of small angle of short length (SASL), we enlarge the QC of the blurred image by a magnification factor of 2, i.e., twofold QC. Values for the additional pixels in the output spectrum are determined utilizing the bicubic interpolation method^[18]. During the second-pass parameter detection of blur direction, the original pair of central darkest points then move to new coordinates, which are (x'_l, y'_l) for the left point, and (x'_r, y'_r) for the right point. In such a way, for the situation of the SASLP, the formula for identifying the blur angle turns out to be

$$\theta' = \arctan\left(\frac{y'_r - y'_l}{x'_r - x'_l}\right),$$

$$\theta \in \left(-\frac{\pi}{2}, -\frac{4\pi}{9}\right] \cup \left[-\frac{\pi}{18}, 0\right) \cup \left(0, \frac{\pi}{18}\right]$$

$$\cup k\left[\frac{4\pi}{9}, \frac{\pi}{2}\right), \quad L \leq 15. \quad (36)$$

It needs our attention that the maximal identifiable motion length via QQ technique would reach half the diagonal of the image, as long as the QTPM are containable within the QC. For instance, if the directional angle of the PSF is $\theta = 0$, then the maximal identifiable motion length is $L = \frac{X}{2}$; if the directional angle of the PSF is $\theta = \frac{\pi}{2}$, then the maximal identifiable motion length is $L = \frac{Y}{2}$; if the directional angle of the PSF is $\theta = \pm \arctan \frac{Y}{X}$, then the maximal identifiable motion length is $L = \frac{\sqrt{X^2 + Y^2}}{2}$, which is just the half of the

image diagonal.

6 Experiments

6.1 Blur Kernel Identification

6.1.1 Via Frequency Domain

To visualize and validate our derivation, we supply two groups of experiments with MATLAB tools, and concrete data are listed in Table 1. The first group of data are for special cases, such as $\theta = 0$, $\theta = \frac{\pi}{2}$ or $P = Q$; the second group are for experiment in general cases. In both experiments, the input parameters are (θ, L, P, Q) , the intermediate variables are (ϕ, d, ψ) , and the output parameters are (θ, L) . We generate the ULMB kernels using assigned (θ, L) (as described in Subsections 2.3), and perform the DFT on each of them with assigned (P, Q) (as described in Subsection 4.2.1). The zero-frequency component is shifted to the center of each AS, the pixel intensities of which are then normalized to $[0, 1]$.

The parameters ϕ and d are decided in two ways. The first way is by measuring AS stripes. When we perform the Radon transform on the AS for the angle in range of $(-\frac{\pi}{2}, \frac{\pi}{2}]$, the maximum value of the transformed result indexes the angle ϕ . Then, we rotate the AS for the angle of $-\phi$. By summing the pixel values of row vectors, a curve is formed, and d is half of the distance between the first pair of minima that are symmetrically adjacent to the central maximum. Measured values are displayed in the column of M (measured result). We also directly calculate (ϕ, d) according to (22) and (31), as displayed in the column of C (calculated result), for the purpose of seeing whether the measured results cohere with our calculations.

The parameters (θ, L) using measured (ϕ, d) are also estimated by two means. One set of data is acquired on the basis of the predecessors' perpendicular relationship, as displayed in the column of the first P (predecessors' result). The other set of data is calculated by applying our formulas in (32), as displayed in the column of the first O (our result). We will check whether

Table 1. Concrete Experimental Data (Frequency Domain)

G	θ, L, P, Q	ϕ, d		$E \theta, L$		ψ		
	S	M	C	P	O	P	A	O
1	0, 21, 256, 128	90, 12	90, 12.19	0, 21.33	0, 21.33	± 90	-90	-90
	90, 21, 128, 256	0, 12	0, 12.19	90, 21.33	90, 21.33		90	90
	45, 21, 128, 128	-45, 6.50	-45, 6.10	45, 19.69	45, 19.69		90	90
	-45, 21, 128, 128	45, 6	45, 6.10	-45, 21.33	-45, 21.33		-90	-90
2	45, 21, 256, 128	-26, 8	-26.57, 7.71	64, 32/16	45.71, 20.09		71.57	71.57
	45, 21, 128, 256	-64, 8	-63.43, 7.71	26, 16/32	44.29, 20.09 ¹		108.43	108.43
	-45, 21, 256, 128	26, 8	26.57, 7.71	-64, 32/16	-45.71, 20.09		-71.57	-71.57
	-45, 21, 128, 256	64, 8	63.43, 7.71	-26, 16/32	-44.29, 20.09		-108.43	-108.43

Note: G-Group number, E-Estimated, S-Synthetic result, M-Measured result, C-Calculated result, P-Predecessors' result, O-Our result, A-Algebraic result. All the angles are recorded in degrees. The values at the left and the right side of "/" are estimated by (8) and (9), respectively.

each group of output parameters equal their true values.

With simulated θ and measured ϕ at hand, the value of ψ is already clear. We compare the results in three different facets that are produced. The first is indicated by the relation of perpendicularity, which will be always $\psi = \pm \frac{\pi}{2}$, as displayed in the column of the second P (predecessors' result). The second is approached algebraically using (23), as displayed in the column of A (algebraic result). We finally calculate ψ via (24), as displayed in the column of the second O (our result).

1) *Special Cases.* While these cases have been well demonstrated in previous literature, we still provide four examples for comparisons, which include the situations of $\theta = 0$, $\theta = \frac{\pi}{2}$, and $P = Q$, respectively. Assign (θ, L, P, Q) to $(0, 21, 256, 128)$, $(\frac{\pi}{2}, 21, 128, 256)$, $(\frac{\pi}{4}, 21, 128, 128)$, and $(-\frac{\pi}{4}, 21, 128, 128)$, respectively. Fig.4 shows the results, in which the parameters with the kernel are (θ, L) and those with each corresponding AS are (P, Q) , respectively.

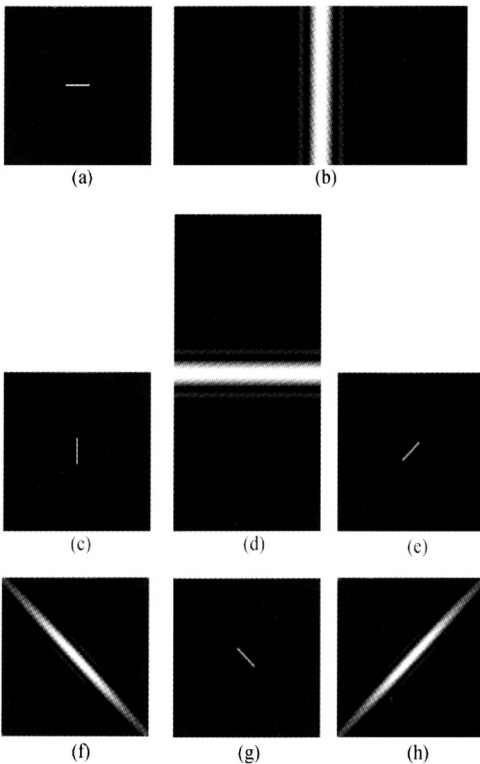


Fig.4. Four examples of special cases. (a) Kernel, $(0, 21)$. (b) AS, $(256, 128)$. (c) Kernel, $(\frac{\pi}{2}, 21)$. (d) AS, $(128, 256)$. (e) Kernel, $(\frac{\pi}{4}, 21)$. (f) AS, $(128, 128)$. (g) Kernel, $(-\frac{\pi}{4}, 21)$. (h) AS, $(128, 128)$.

2) *General Cases.* We provide four examples. In the first two examples, we assign (θ, L) to $(\frac{\pi}{4}, 21)$, and assign (P, Q) to $(256, 128)$ and $(128, 256)$, respectively. In the last two examples, assign (θ, L) to $(-\frac{\pi}{4}, 21)$, and

assign (P, Q) to $(256, 128)$ and $(128, 256)$, respectively. Fig.5 shows the results, in which the parameters with the kernel are (θ, L) and those with each corresponding AS are (P, Q) , respectively.

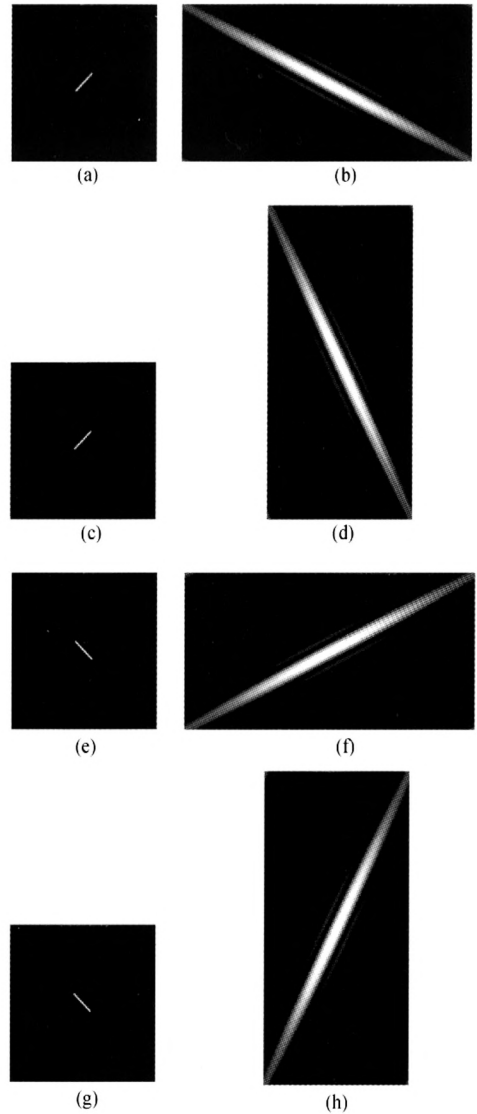


Fig.5. Four examples of general cases. (a) Kernel, $(\frac{\pi}{4}, 21)$. (b) AS, $(256, 128)$. (c) Kernel, $(\frac{\pi}{4}, 21)$. (d) AS, $(128, 256)$. (e) Kernel, $(-\frac{\pi}{4}, 21)$. (f) AS, $(256, 128)$. (g) Kernel, $(-\frac{\pi}{4}, 21)$. (h) AS, $(128, 256)$.

In the experiments, we choose $\theta = \pm \frac{\pi}{4}$ as the instance since it is easy to directly view the inclination tendency of AS stripes with respect to the input parameters (θ, L, P, Q) . All the measured values conform to what we have deduced in Subsection 4.2, and the estimated motion parameters by our formulas match actual values with acceptable errors.

6.1.2 Via QQ Domain

Generate a series of blurred Baboon images and recognize their kernels in accordance with procedures in Subsection 5.2.

1) Images Without Noise

Experimental angles of motion blur are arranged in $(-90, 90]$ degrees at an interval of 15; the lengths are arranged in $[5, 125]$ pixels at an interval of 10. These parameter combinations total up to 169 datasets. We compare the identification errors, respectively, of motion length and motion direction, by subtracting each value of synthetic parameters from its corresponding estimated value. The errors may be positive or negative, as shown in Fig.6(a). We draw the distributions of statistic histograms for identification errors of motion length and motion direction, respectively, as shown in Fig.6(b). From it, length identification errors of all the tested data are within $(-1, 1)$ pixel, and errors of most angle identifications are within $(-1, 1]$ degree, which manifests high reliability for clean images.

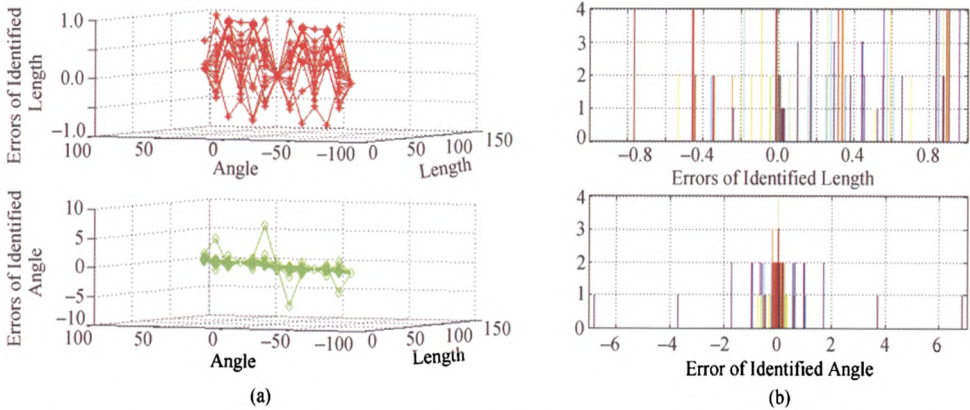


Fig.6. Kernel identification errors of synthetic clean Baboons. (a) Datasets. (b) Statistic histograms.

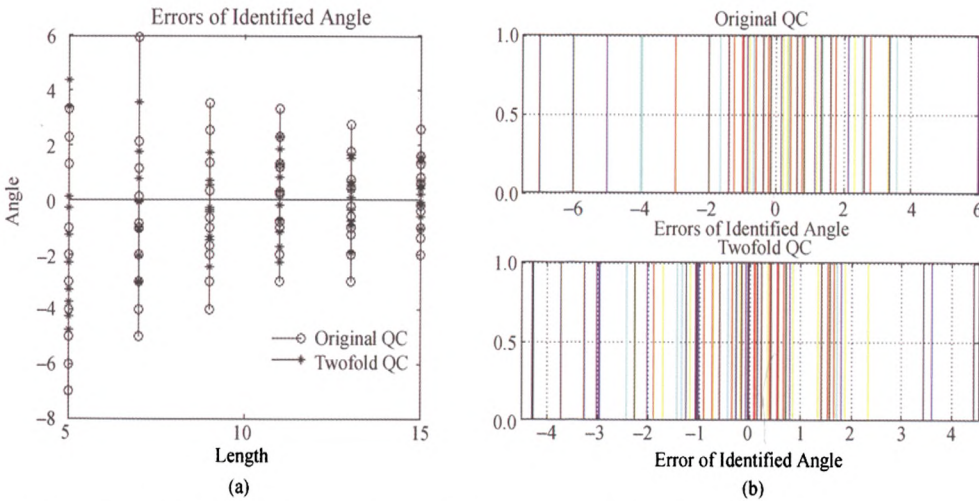


Fig.7. Kernel angle identification errors of twofold QC vs original QC. (a) Datasets. (b) Statistic histograms.

Toward the SASLP, we test another 60 datasets of the blurred Baboon images. As experiments, we directed detect blur parameters by twofold QC of one pass QC. The blur angles of the PSF are arranged in $[1, 10]$ degrees at an interval of 1, whose pertinent blur lengths fall in between $[5, 15]$ pixels at an interval of 2. Seen from Fig.7(a), coordinates of error points identified by twofold magnified QC locate much closer to zero-valued horizontal axis. This trend is revealed according to Fig.7(b), too. These testing results imply that the angle errors for identifying the SASL kernels are reduced by the technique via twofold magnified QC. This complies with the analysis on sampling rate, and the magnification of the spectral graph contributes to multiply the number of sampling points along the blur length for a finer representation of the blur-angle information.

2) Noisy Images

It should be emphasized that noise detection and noise removal are beyond the scope of our paper, and we

only discuss the noisy situation in possible noise-resistance conditions. We measure the image quantity by the signal-to-noise ratio (SNR)^[9], which is defined as

$$\text{SNR} = 10 \log \frac{\text{var}(\text{signal})}{\text{var}(\text{noise})}, \tag{37}$$

where $\text{var}(\cdot)$ stands for the variance value, and the signal here refers to the clean image. We add Gaussian noise to generate noisy blurred images of $\text{SNR} = 10 \text{ dB}$. Experimental angles of motion blur are arranged in $[-45, 45]$ degrees at an interval of 15; the lengths are arranged in $[15, 75]$ pixels at an interval of 10. These parameter combinations total up to 49 datasets. The identification errors of noisy images and its relevant statistic histograms are shown in Fig.8. From it, most of the identification errors for angle are within the range

of $[-2, 2)$ degrees, and those for length are within the range of $[-2, 2)$ pixels. The QC technique is relatively reliable for $\text{SNR} = 10 \text{ dB}$ noisy images.

6.2 Blurred-Image Restoration

An important application of blur-kernel recognition is image reproduction, viz. utilizing the estimated blur to deblur an image. As analyzed in Section 5, we choose the QQ domain technique for kernel recognition to restore collected images from actual scenarios, rather than the AS or the cepstrum techniques.

Figs.9(a) and 9(d) are four snapshots of the ULMB captured without flash by a Nikon Coolpix S700 camera, and their sizes (in a left-to-right and top-to-bottom sequence) are 1000×870 , 845×690 , 782×538 , and 753×346 . We first recognize their kernels using the QC

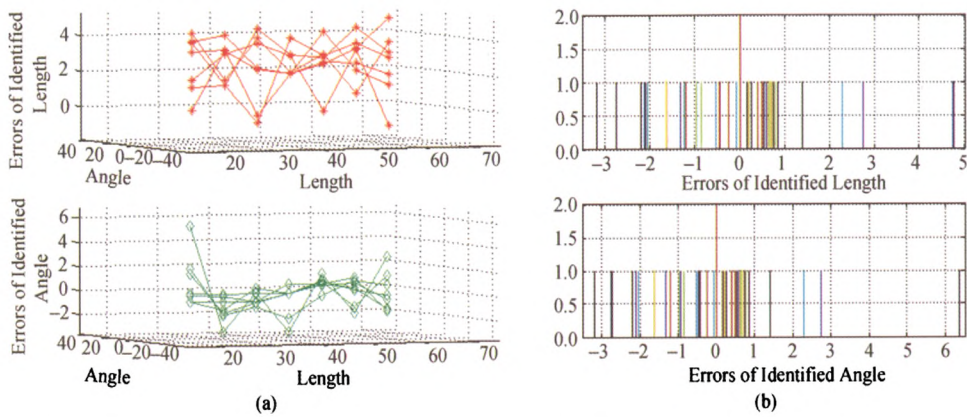


Fig.8. Kernel identification errors of synthetic noisy Baboons. (a) Datasets. (b) Statistic histograms.

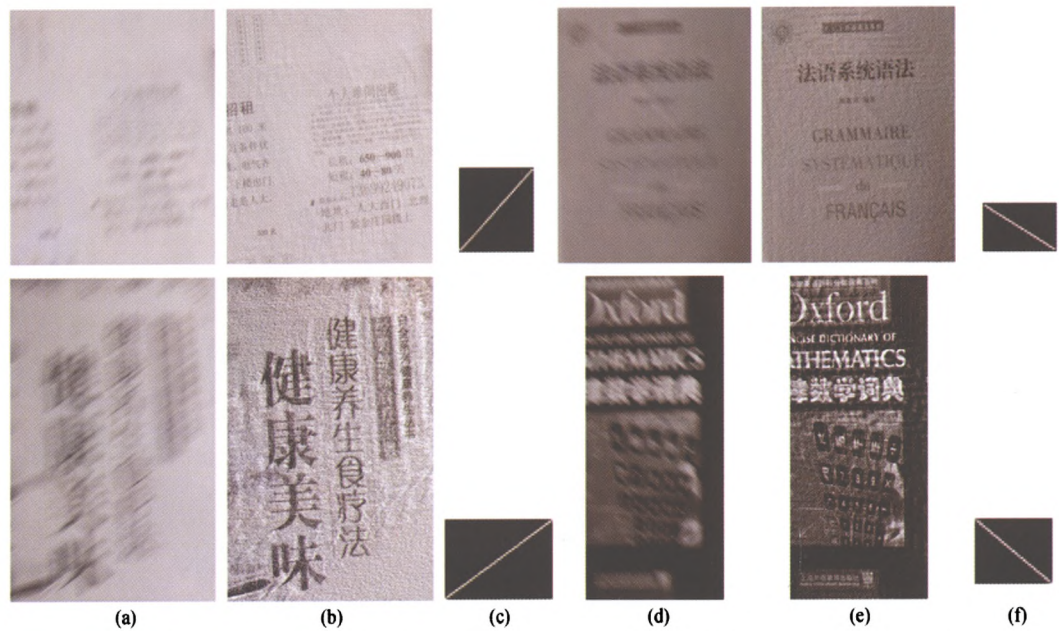


Fig.9. Actual image estimations via QC technique. (a) Blurred. (b) Restored. (c) Identified. (d) Blurred. (e) Restored. (f) Identified.

QC identification technique and then recover them using the deblurring approach of Levin *et al.*^[19]. The kernels recognized are $(\theta_1, L_1) = (45.71, 57.28)$, $(\theta_2, L_2) = (-30.21, 45.71)$, $(\theta_3, L_3) = (33.92, 68.09)$, and $(\theta_4, L_4) = (-37.88, 45.61)$, as shown in Figs. 9(c) and 9(f), and the restored images are shown in Figs. 9(b) and 9(e). The results show that important details of photos are well recovered.

6.3 Discussions

In Section 5, we indicated the limitations of AS and cepstrum methods, and images in variant scenarios are visualized by Fig. 3. The experimental comparison of AS and cepstrum against QC, in Subsection 6.1, favorably highlights the superiority of the QC approach. The superiority for the blur-kernel detection includes its ability to help relieve the SASLP and its better noise resistance.

Despite these merits, we have to acknowledge two potential limitations of our current QC-oriented approach.

1) On the Super-SASLP (SSASLP)

There exist several possible scenarios for ULMB images, and our framework succeeds somewhere but fails otherwise. Refer to Table 2 to learn more.

Table 2. Demonstration of Success and Failure

Scenarios	L		
	Large	Small	Super-Small
$\theta(\theta')$			
Large	1	1	1
Small	1	2	N
Super-Small	1	N	N

Note: 1 – one-pass QC approach succeeds;

2 – two-pass twofold QC approach succeeds;

N – neither approach succeeds.

For motion direction, we specify the measurement of *large* or *small* indicates the inclination level of angles against the axis, horizontal or vertical. In the context, all the angles are recorded in degrees, and all the lengths in pixels. For simplicity, large angles denote the angle in range of $(10, 45]$, small angles in $(5, 10]$, and super-small angles in $(0, 5]$. Specifically, large angles stand for the motion direction in range of $(-80, -10] \cup (10, 80)$, small angles in $(-85, -80] \cup [-10, -5] \cup (5, 10] \cup [80, 85]$, and super-small angles in $(-90, -85] \cup [-5, 0] \cup (0, 5] \cup [85, 90)$. Exclusive situations of 0 and 90 are a usual success for one-pass QC approach. For motion length, large lengths represent the motion length in range of $(15, \frac{\sqrt{X^2+Y^2}}{2})$, small lengths in $(5, 15]$, and super-small lengths in $(0, 5]$.

The SSASLP is more challenging, although these slight deviations do not degrade the image much or would not necessarily need further processing. But in some particular cases, the images that approach high definition are required.

2) On the Noise

In Subsection 6.1.2, the SNR of synthetic noisy blurred images is 10dB, measured by (37). If the noise level increases much, current QC framework will fail, either. In this circumstance, some remedy solutions will be required.

7 Conclusions

Although ULM is a primitive form of motion, topics of its blur identification and image restoration remains popular. An identifying principle rooted in Fourier AS proposed in Cannon's paper is still in use today, and it invokes our new thinking.

We supplied elaborate derivations of the generalized Fourier frequency phase form and AS properties, and experimental results are consistent with deduced formulas. At the same time, we put forward a revised cepstrum, namely, the quasi-cepstrum, to overcome disadvantages of the ULMB detection in frequency and standard cepstrum domains. Through this revision, the blur-kernel recognition not only becomes more straightforward, swifter and more efficient, but also leads to lower errors and higher immunity to noise. Moreover, our proposed one-pass and two-pass methods on the basis of the QC help relieve the identification problems of oversized and undersized ULMB kernels. The improved QC-based approaches are applicable to real-world collected images as well as the synthetic blurred, and thus are more beneficial to remove the ULMB from images.

In spite of this, a more precise method is expected to deal with the SASLP, especially in a poorer condition that involves much noise in the image.

References

- [1] Slepian D. Restoration of photographs blurred by image motion. *Bell System Technology Journal*, 1967, 46: 2353-2362.
- [2] Yitzhaky Y, Kopeika N S. Identification of blur parameters from motion blurred images. *Graphical Models and Image Processing*, 1997, 59(5): 310-320.
- [3] Chen Q R, Lu Q S, Cheng L Z. Identification of the motion blurred direction of motion blurred images. *Journal of National University of Defense Technology*, 2004, 26(1): 41-45. (in Chinese)
- [4] Moghaddam M E, Jamzad M. Finding point spread function of motion blur using Radon transform and modeling the motion length. In *Proc. the 4th IEEE International Symposium on Signal Processing and Information Technology*, Roma, Italy, Dec. 18-21, 2004, pp.314-317.
- [5] Dobes M, Machala L, Furst T. Blurred image restoration: A fast method of finding the motion length and angle. *Digital Signal Processing*, 2010, 20(6): 1677-1686.
- [6] Lokhande R, Arya K V, Gupta P. Identification of parameters and restoration of motion blurred images. In *Proc. the 21st Annual ACM Symposium on Applied Computing*, Dijon, France, Apr. 23-27, 2006, pp.301-305.
- [7] Dash R, Sa P K, Majhi B. RBFN based motion blur parameter estimation. In *Proc. 2009 International Conference on*

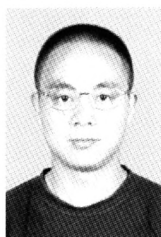
Advanced Computer Control, Singapore, Singapore, Jan. 22-24, 2009, pp.327-331.

- [8] Cannon M. Blind deconvolution of spatially invariant image blurs with phase. *IEEE Transactions on Acoustics, Speech, and Signal Processing*, 1976, 24(1): 58-63.
- [9] Fabian R, Malah D. Robust identification of motion and out-of-focus blur parameters from blurred and noisy images. *Graphical Models and Image Processing*, 1991, 53(5): 403-412.
- [10] Wu S Q, Lu Z K, Ong E P, Lin W S. Blind image blur identification in cepstrum domain. In *Proc. the 16th International Conference on Computer Communications and Networks*, Honolulu, USA, Aug. 13-16, 2007, pp.1166-1171.
- [11] Xie W, Qin Q Q. Estimating blur parameters of point spread function of motion blurred image based on Cepstrum. *Geomatics and Information Science of Wunan University*, 2008, 33(2): 128-131. (in Chinese)
- [12] Chang M M, Tekalp A M, Erdem A T. Blur identification using the bispectrum. *IEEE Transactions on Signal Processing*, 1991, 39(10): 2323-2325.
- [13] Yoshida Y, Horiike K, Fujita K. Parameter estimation of uniform image blur using DCT. *IEICE Transactions on Fundamentals of Electronics, Communications and Computer Sciences*, 1993, E76(7): 1154-1157.
- [14] Ahmed N, Natarajan T, Rao K R. Discrete cosine transform. *IEEE Transactions on Computers*, 1974, 23(1): 90-93.
- [15] Oppenheim A V, Schaffer R W. Discrete-Time Signal Processing, 3rd edition. Upper Saddle River, New Jersey: Prentice-Hall, Inc, 2009.
- [16] Gonzalez R C, Woods R E. Digital Image Processing, 3rd edition. Upper Saddle River, New Jersey: Prentice-Hall, Inc., 2008.
- [17] Polyanin A D, Manzhirov A V. Handbook of Mathematics for Engineers and Scientists. Boca Raton, Florida: Chapman and Hall/CRC Press, 2006.
- [18] Keys R. Cubic convolution interpolation for digital image processing. *IEEE Transactions on Acoustics, Speech, and Signal Processing*, 1981, 29(6): 1153-1160.

- [19] Levin A, Fergus R, Durand F, Freeman W T. Image and depth from a conventional camera with a coded aperture. *ACM Transaction of Graphics*, 2007: 26(3).



Lu Wang is a Ph.D. candidate at the Institute of Automation, Chinese Academy of Sciences (CASIA). Her research interest is in digital image processing.



Hong-Yan Zhang is a lecture at the Sino-European Institute of Aviation Engineering, Civil Aviation University of China. He received his Ph.D. degree from the CASIA in 2011. His research interests include computer vision, image processing, aviation engineering and quantum information theory.



Si-Long Peng is a professor at the CASIA. He received his Ph.D. degree from the Institute of Mathematics, CAS in 1998. His research interests include digital image processing, wavelets analysis, and multirate signal processing.